Numerical and experimental comparison of confinement effects on a Fully-Passive Oscillating-Foil Turbine

K. Gunther[1], S. Mann[2], G. Dumas[1]*, P. Oshkai[2]

[1]CFD Laboratory LMFN, Département de génie mécanique, Université Laval, Québec, Canada
[2]Department of Mechanical Engineering, University of Victoria, Victoria, Canada
*Corresponding author: guy.dumas@gmc.ulaval.ca

Abstract—A numerical and experimental comparison of a fully-passive oscillating-foil turbine operating in different confinement levels is conducted to assert how well CFD-based FSI simulations can predict the performances of the turbine. It is found the present 3D URANS simulations match reasonably well the experimental observations, especially in terms of pitch angles and power extraction. Indeed, the results confirm that confinement increases the extracted power and the efficiency of the fully-passive blade. At low confinement level, the main flow features are shown to be well captured by the simulations. At large confinement levels, some issues with lateral walls interactions are discussed as possible explanation for the observed discrepancies.

Fully-passive oscillating foil; fluid-structure interaction; confinement

I. INTRODUCTION

The oscillating-foil turbine (OFT) is one of the many existing concepts to extract energy from the flow of water. This turbine consists of a rectangular foil oscillating in a combined pitch and heave motion. In the initial version of the concept, the kinematics of the foils was completely constrained, imposing given values for the heaving and pitching amplitudes, the frequency and the phase. Unfortunately, coupling and constraining the motions in heave and pitch comes at the cost of mechanical complexity [1]. This inherently raises reliability concerns and causes excessive energy loss in friction.

A solution is to let both degrees of freedom respond freely to the FSI between the flow and the foil (Veilleux and Dumas [2]). By adjusting appropriately, the stiffness of springs, the inertia of the moving components and the resistive force of a generator, the passive foil can experience regular motions of large amplitudes that are completely controlled by an exchange of energy between the fluid and the foil. Thus, the need of a complex mechanism is eliminated. We refer to this version of the concept as "fully-passive" OFT as opposed to "constrained OFT".

One main advantage of the OFT is its rectangular energy extraction area. This is ideal for large and shallow rivers since the turbine can have a larger frontal area compared to horizontal axis turbines, where the width and height are equal to its diameter.

In most numerical studies of the fully-passive OFT, the turbine is set to operate in a very large domain in order to be independent of confinement effects. It is known that for constrained OFT (Gauthier et al. [3]) and other types of turbine (Ross and Polagye [4], Kinsey and Dumas [5]), increasing the confinement level increases also the energy extraction performances by forcing more flow through the extraction plane. However, this has not yet been demonstrated for fully-passive OFT. Since the motions of the foil are highly dependent on the flow, it is important to confirm that the turbine can be operated in confined conditions, especially if it is destined to be operated in rivers.

Several numerical studies of the fully-passive OFT have been conducted, but there is very few experimental comparisons and validations. To resolve this issue, a numerical and experimental comparison of confinement effects is conducted at Reynolds number 19 000. This comparison will serve to assert if a URANS-based FSI solver can capture the same trends as those obtained on an experimental prototype. Also, this study verifies if increasing confinement levels on a fully-passive OFT with given structural parameters optimized for an unconfined flow will indeed increase its performances and maintain stable and periodic motions.

II. EXPERIMENTAL SYSTEM AND TECHNIQUES

A. Modeling the fully-passive OFT

The present fully-passive OFT consists of a rectangular NACA 0015 foil with an aspect ratio of 7.5. The pitch axis x_p is located one-third of the chord downstream from the leading edge. The pitch axis heaves with $h(t)$ and pitches with $\theta(t)$. A schematic of the prototype is presented in Figure 1.

The turbine has components, such as the chariot, moving in heave only with a total mass identified as $m_{translation}$ and are represented by the yellow block. Other components, mounted on the chariot such as the foil, can rotate. These have a mass identified as m_θ, The center of mass of the rotating components

is located on the chord line at a distance x_θ from the pitch axis, where x_θ is positive in the downstream direction, as indicated by the arrow in Figure 1. The product of x_θ and m_θ yields a single parameter called the static moment S, which couples the heaving and pitching motions together and allows energy transfer from one degree of freedom to the other. The total mass in heave m_h is the sum of m_θ and $m_{translation}$. The moment of inertia I_θ in rotation depends on the mass distribution and the location of the pitch axis x_p.

To model the presence of an electric generator connected to the heave motion, it is assumed that its resistive force is proportional to velocity, so that it can be directly modeled as a viscous damper with a damping coefficient of $D_{h,e}$. On the experimental prototype, two kinds of friction are present: dry Coulomb friction $C_{Fy, Coul}$ and viscous friction $D_{h,v}$. In the numerical model, the total viscous damping coefficient D_h is the sum of $D_{h,e}$ and $D_{h,v}$. On the prototype, no generator is used in pitch, there are only dry friction $C_{M, Coul}$ and viscous friction D_θ.

For each degree of freedom, springs with a stiffness of k_θ and k_h respectively in pitch and heave are used to maintain the oscillations around an equilibrium position.
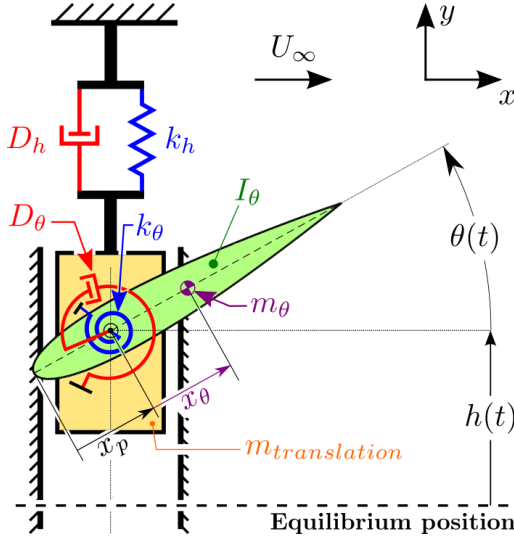

Figure 1: Schematic of the fully-passive OFT

The different parameters are normalized in the following way:

$$m_h^* = \frac{m_h}{\rho b c^2} \qquad h^* = \frac{h}{c} \qquad I_\theta^* = \frac{I_\theta}{\rho b c^4} \qquad \theta^* = \theta$$

$$D_h^* = \frac{D_h}{\rho U_\infty bc} \qquad \dot{h}^* = \frac{\dot{h}}{U_\infty} \qquad D_\theta^* = \frac{D_\theta}{\rho U_\infty bc^3} \qquad \dot{\theta}^* = \frac{\dot{\theta}c}{U_\infty}$$

$$k_h^* = \frac{k_h}{\rho U_\infty^2 b} \qquad \ddot{h}^* = \frac{\ddot{h}\,c}{U_\infty^2} \qquad k_\theta^* = \frac{k_\theta}{\rho U_\infty^2 bc^2} \qquad \ddot{\theta}^* = \frac{\ddot{\theta}\,c^2}{U_\infty^2}$$

$$C_{Fy,Coul} = \frac{F_{y,Coul}}{\rho\, U_\infty^2 bc} \quad S^* = \frac{S}{\rho bc^3} \quad C_{MCoul} = \frac{M_{Coul}}{\rho\, U_\infty^2 bc^2}$$

$$C_y = \frac{F_y}{\rho\, U_\infty^2 bc} \qquad Re = \frac{\rho U_\infty c}{\mu} \qquad C_M = \frac{M}{\rho\, U_\infty^2 bc^2}$$

The dynamical equations governing the motions of the foil are given by:

$$\frac{C_y}{2} = m_h^* \ddot{h}^* + D_h^* \dot{h}^* + k_h^* h^* + C_{Fy,Coul}$$
$$+ S^* \left(\ddot{\theta}^* \cos(\theta^*) + (\dot{\theta}^*)^2 \sin(\theta^*) \right) \tag{1}$$

$$\frac{C_M}{2} = I_\theta^* \ddot{\theta}^* + D_\theta^* \dot{\theta}^* + k_\theta^* \theta^* + S^* \ddot{h}^* \cos(\theta^*) + C_{MCoul} \tag{2}$$

which show the coupling between the motions and the driving action of the hydrodynamic forces and moment applied on the foil.

To calculate the mean power coefficient, only the energy transferred to the generator $C_{Ph,e}$ is accounted for. Its mean value $\overline{C_{Ph,e}}$ is averaged over the period T at each cycle i.

$$\overline{C_{Ph,e}} = \frac{2}{T} \int_{t_i}^{t_i+T} D_{h,e} \left(\dot{h}^* \right)^2 \ dt \tag{3}$$

A simple conversion factor with the mean height swept by the foil, d, gives the mean efficiency coefficient $\overline{\eta_e}$.

$$\overline{\eta_e} = \overline{C_{Ph,e}} \ \frac{c}{d} \tag{4}$$

The swept height d reflects the maximum and minimum distance in the y direction reached by any part of the foil. This is typically larger than the maximum heave amplitude H_0. Most often, it is the trailing edge that reaches the maximum swept distance.

Consistent with the definition proposed by Gauthier et al. [3] and used by Mann et al. [6], the mean confinement level is defined as:

$$\bar{\varepsilon} = \frac{A_t}{A} = \frac{2\overline{H_0}}{H} \frac{b}{W} \tag{5}$$

where A_t is the extraction area of the turbine, itself defined as the product of the span of the blade b and twice the heaving amplitude $\overline{H_0}$. The cross-section area A of the channel is simply the product of its height H and width W.

However, the extraction area of a fully-passive OFT depends on $\overline{H_0}$ which varies with the confinement level, thus $\overline{H_0}$ is an unknown. Plus, in this confinement study, only the height H of the channel is changed. In this perspective, a characterization of the confinement that is independent of the results is used here by taking the ratio c/H ($c/H \rightarrow 0$ for unconfined condition).

The four main metrics describing the motion of the foil are expressed by:

$$f_i^* = f_i \frac{c}{U_\infty} \tag{6}$$

$$\phi_i^* = \frac{360°}{T_i} \left(t_{\theta max,i} - t_{h max,i} \right) \tag{7}$$

$$H_{0,i}^* = \frac{h_{max,i} - h_{min,i}}{2c} \tag{8}$$

$$\theta_{0,i}^* = \frac{\theta_{max,i} - \theta_{min,i}}{2} \tag{9}$$
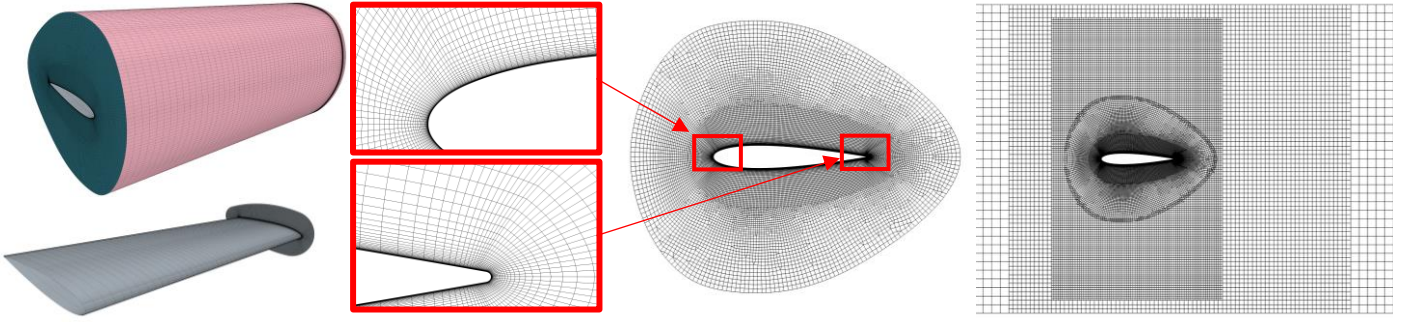
Figure 2: Illustration of the overset and background mesh

The amplitude $H_{0,i}^*$ is calculated by taking the difference of the maximum and minimum heave position $h(t)$ of the pitch axis through cycle i. The phase ϕ_i^* is measured by taking the difference between the time at which the maximum pitching and maximum heaving occur. A positive phase means that the maximum pitching amplitude occurs after the maximum heaving amplitude, whereas a negative phase means that the maximum pitching occurs before the maximum heaving amplitude.

The structural parameters used in this study are presented in Table 1. Uncertainty is present in the measurements of the structural parameters applied to the prototype. Despite possible slight discrepancies between the numerical and the experimental parameters $\left(D_h^*;\ D_\theta^*;\ C_{Fy,Coul};\ C_{M_{Coul}}\right)$, it is assumed to have a negligeable impact on the comparison of the results and on the present conclusions.

TABLE I.   STRUCTURAL PARAMETERS USED IN THE NUMERICAL
SIMULATION AT $Re = 19\,000$

Parameter	Value	Parameter	Value
m_h^*	3.65	I_θ^*	0.098
D_h^*	1.1505	D_θ^* *	0.002
k_h^*	2.08	k_θ^*	0.056
$C_{Fy,Coul}$	0.05	$C_{M_{Coul}}$	0.02
S^*	0.043	x_P/c	1/3

B. Numerical setup

The experimental OFT consists of a NACA 0015 rectangular blade with a 50 mm chord and a span b of 7.5 chords. The turbine is centered in x-y plane. In still water, the dept of water is 8.4 chords. There is a small gap of 0.1 chord between the blade's plate and the bottom of the channel. The channel has a cross section of 9 chords by 9 chords and a length of 50 chords. To impose the confinement, false walls parallel to the x-z plane are inserted in the channel. To increase the confinement level, the walls are slid closer together. For more details on the experimental setup and the PIV measurements, the reader can refer to the papers from Mann et al. [6], Iverson [7] and Boudreau et al. [8].

The present numerical simulations aim mainly to reproduce the critical physics at play in the experiments, namely the 3D and

confinement effects. At the same time, simplifications in the numerical simulations are needed to lighten the calculations, such as ignoring the surface deformation and the boundary layers on the walls of the channel (slip walls). Moreover, only half of the turbine span is modeled by using a symmetry plane in the middle of the blade, as shown in Figure 3. Thus assuming that the turbine physics is symmetrical in the spanwise direction, only the bottom half of the prototype is considered, including the gap of 0.1 c between the endplate and the channel floor, as illustrated horizontally in Figure 3.
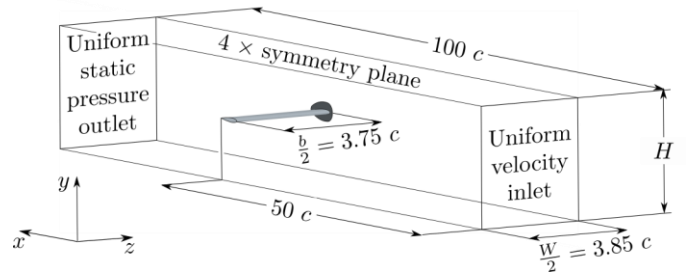

Figure 3: Schematic of the numerical channel with half the oscillating blade

The boundary conditions used in the numerical model are illustrated in Figure 3. A uniform velocity profile is set at the inlet, 50 chords upstream of the turbine. A uniform static pressure outlet is imposed 50 chords downstream. Slip walls are used for the channel, thus ignoring the boundary layers and the viscous interactions next to the blade's tip. To modify the confinement level, the height H of the domain is changed accordingly to the values used in the experimental campaign.

The numerical simulations are carried out using Siemens Star-CCM+ 2021.2, version 16.04.007 . The overset-mesh technique is used, which consists of one stationary mesh for the background and one mobile mesh around the foil. The background mesh modeling the channel uses 808 008 trimmed cells. As shown in Figure 2, the trimmed cells have approximately the same size as the exterior cells of the overset mesh. Where the foil oscillates, there is a refined zone of trimmed mesh. Its resolution is relaxed further away from the turbine. For the mobile overset-mesh, illustrated in Figure 2 with the pink and blue surfaces, 3 843 251 cells are used, with 366 nodes surrounding the foil's section in the x-y plane. To maintain a y^+ value below 1, the first cells surrounding the foil have a thickness of 5.1×10^{-6} c. An expansion coefficient of 1.2 is used with a geometric law. In Figure 2, the expansion of the cells thickness is shown at the leading and trailing edges. Structured mesh is used from the foil's surface to the edge of the

plate, and free mesh is used elsewhere. The mesh is extruded in the z direction with a 0.08 c spacing with 41 cells. Near the tip, the mesh spacing in the z direction is reduced on a distance of 0.46 c with a maximum contraction rate of 1.2 . The endplate in the simulation has no thickness, but it has an identical shape as the one on the prototype. The present mesh discretization is similar to that of Kinsey and Dumas [9] with their fully constrained OFT.

The simulations are carried out using 3D incompressible Unsteady Reynolds-Averaged Navier-Stokes (URANS) in combination with of the Spalart-Allmaras one-equation turbulence model. At the inlet, the modified turbulent viscosity ratio $\tilde{v}/v = 3$ is set. Second-order numerical schemes are used in both spatial and temporal resolutions. A segregated approach using the SIMPLE algorithm is chosen for the pressure-velocity coupling. A convective time step $\Delta t\, U_\infty/c$ of 0.005 is used, which represents over 1500 timesteps per cycle. For the initial conditions, the flow field from a stationary RANS simulation is used with the blade centered but pitched at 0.17 radians (~10°). Such physically realistic initial conditions help the fluid-structure algorithm to converge at the first timestep.

For the fluid solver, a convergence criterion based on the hydrodynamic coefficients C_x, C_y and C_M is monitored. Once the absolute value of C_x, C_y and C_M changes by less than 10^{-3} after five fluid iterations, the forces on the blade are considered as converged.

To update the positions in heave and pitch resulting from the forces, an in-house solid-solver based on Broyden's method is used. See Boudreau et al. [10] and Olivier and Paré-Lambert [11] for more details on how this method is implemented and validated. Convergence is reached once the absolute values of the residues from the dynamical equations (1) and (2) become smaller than 10^{-3}.

III. RESULTS

A. Comparison of the metrics

In this section, the CFD and experimental metrics are compared according to their definitions expressed in equations (3) to (9). The goal here is to assess if the present FSI simulations can predict reliably the trends observed experimentally.

Figure 4 shows that both the power coefficient $\overline{C_{P_{h,e}}}$ and the efficiency $\overline{\eta_e}$ increase with the confinement level, except for the experimental data at the highest confinement. Excluding that particular data for the moment, one observes that the trends are well reproduced by the CFD, the power coefficients being within 3% of the experimental values. The larger difference between the numerical and experimental efficiencies is attributed to the fact that $\overline{\eta_e}$ (equation 4) depends on both the power coefficient $\overline{C_{P_{h,e}}}$ and the swept distance d, so slight discrepancies on both of those values compound together to increase the error of the efficiency $\overline{\eta_e}$, which remains quite acceptable (below 9%).

A more important difference in performances appears at $c/H = 0.24$ since on the experimental setup $\overline{\eta_e}$ and $\overline{C_{P_{h,e}}}$ plunges whereas in the FSI simulation, $\overline{\eta_e}$ and $\overline{C_{P_{h,e}}}$ continue to increase. A few hypotheses are currently being investigated to explain that

observation, the most likely being a viscous interaction between the blade's leading edge vortex (LEV) and the lateral wall of the confined channel which is not accounted for in the CFD. This is discussed in more details in the next section.

So we observe that for confinement levels below $c/H = 0.21$, the increase for both metrics follows approximately a linear trend. This is interesting because completely constrained OFTs also see their performances increase linearly with confinement (Gauthier et al. [3]). This suggests that a linear interpolation can be used to estimate the performances of the turbine at any confinement level within a reasonable range. This linear relationship can be obtained simply by testing the turbine at two different confinement levels.
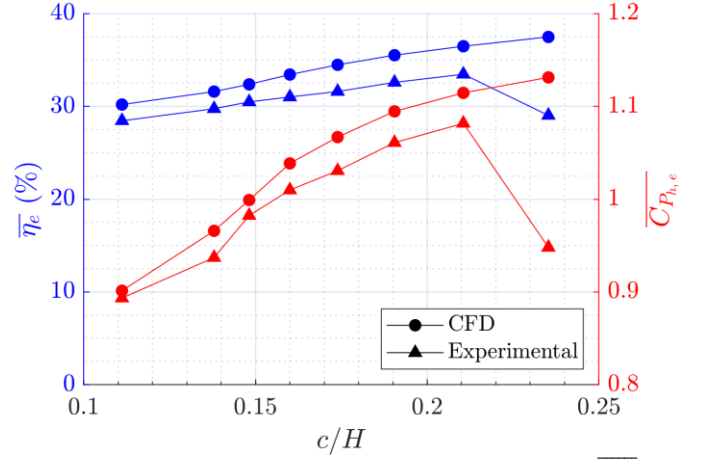

Figure 4: Comparison of the efficiency $\overline{\eta_e}$ and power coefficient $\overline{C_{P_{h,e}}}$.

Looking now at the kinematics of the fully-passive blade, Figure 5 presents the comparison of the observed pitch and heave amplitudes. One can see that pitch amplitudes θ_0^* agree very well and are almost constant close to 80° except for the most confined case. However, the CFD consistently underestimates the heave amplitude $\overline{H_0^*}$ compared to the experimental results. At $c/H = 0.11$, a relative error of 8.0% is present between the CFD and experimental results, but increases up to 18.7% for $c/H = 0.21$, which is significant. More importantly, the two approaches show different trends for $\overline{H_0^*}$: increasing for the experiments and slightly decreasing for the CFD.
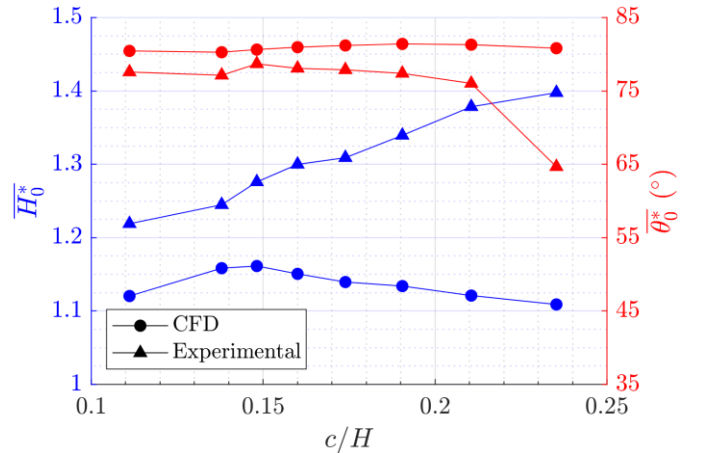

Figure 5: Comparison of the heave $\overline{H_0^*}$ and pitch $\overline{\theta_0^*}$ amplitudes.

At first sight, this behavior of the heave amplitude may seem incoherent with the previously noticed increased of the power coefficients with confinement. This impression would be correct if one assumes that the experimental and numerical oscillations had the same period. Then larger heave amplitudes would be associated to larger velocities of the blade. However, as Figure 6 shows us, the frequency $\overline{f^*}$ tends to decrease in the experiments while it does the opposite in the simulations. Therefore, one must conclude that the increase in performances for $\overline{\eta_e}$ and $\overline{C_{Ph,e}}$ is due to different mechanisms between the two approaches. For the experiments, it is associated to an increase in $\overline{H_0^*}$ while for the CFD, it is due to an increase in frequency.
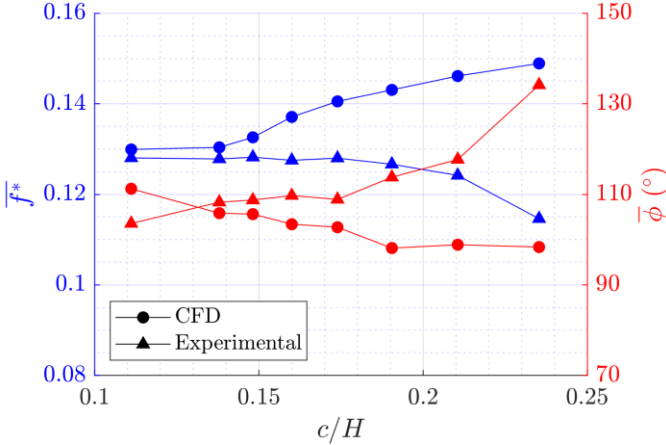

Figure 6: Comparison of the frequency $\overline{f^*}$ and phase $\bar{\phi}$.

At confinement levels below $c/H < 0.148$, the frequencies between the experimental and CFD results are quite similar (better than 2%). Figure 6 also shows that for confinement levels below $c/H < 0.174$, the phase $\bar{\phi}$ differs by less that 7.5%. However, globally, one observes different trends between the experiments and the simulations for both the resulting frequency and the phase lag.

B. Comparison of the flow features

In this section, the normalized vorticity field $\omega_z c/U_\infty$ of the case with a confinement level of $c/H = 0.14$ and $c/H = 0.24$ are compared between the experimental prototype and the CFD simulation. The normalized vorticity field $\omega_z c/U_\infty$ from the CFD and experimental results are taken at $z = b/c = 3.75$, which represents the mid span of the blade. A sequence of pictures during half of a period is presented in Figure 7. Only half of a period is presented since the oscillations are assumed symmetrical. Between each picture in Figure 7, there is a time laps of $1/10^{th}$ of a period which may not correspond exactly to the same time-laps between the experiment and the simulation. The period starts when the pitch axis reaches its maximum position in heave. The goal of this comparison is to visually assert if both methods eject the leading-edge vortex (LEV) at similar times.

The prototype uses PIV measurements to calculate $\omega_z c/U_\infty$, as described by Mann et al. [6]. Since PIV measurements consist of laser sheets tracking the fine particles inside the flow, blind spots occur when objects, such as the foil, block part of the laser sheet. Therefore, some hatching is added on the lower side of the

foil in the experimental sequence of Figure 7. The hatching serves to indicate regions where no experimental visualization was possible. In Figure 7, LEV that is being generated is labelled A, while the one from the previous half-cycle is labelled as B.
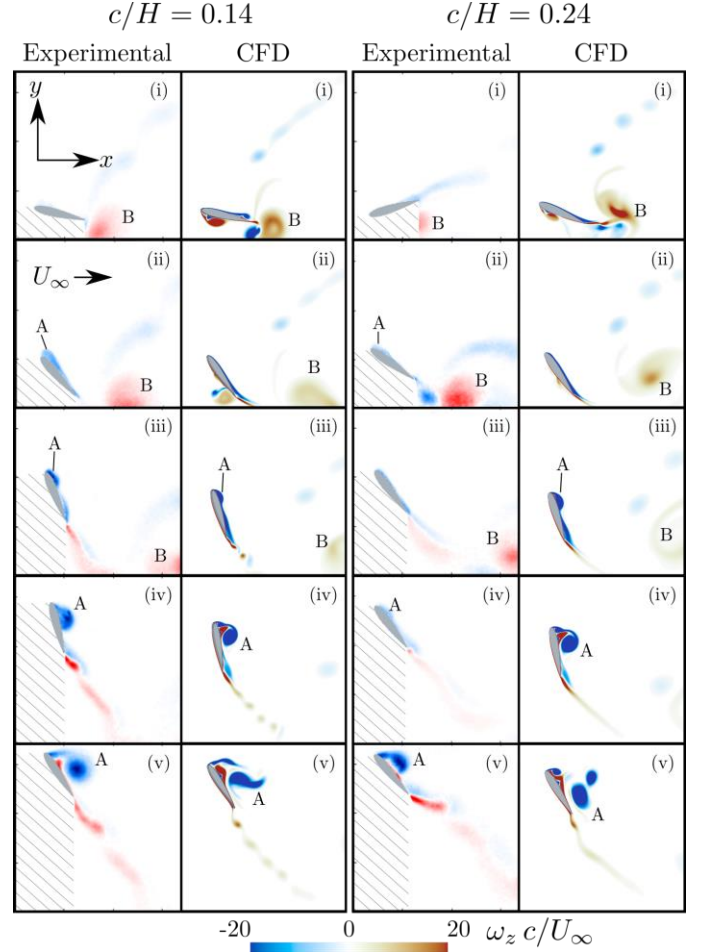

Figure 7: Normalized vorticity fields $\omega_z c/U_\infty$ comparison over half a cycle in low (left) and high (right) confinement levels.

For $c/H = 0.14$, both approaches show similar flow fields. At instant (i), the boundary layer is attached on the upper side of the foil and a LEV B is behind the trailing edge. At that moment, the CFD shows several vortices on the lower side while the experimental image does not show any vorticity there since it's hidden from the PIV. At time (ii), the experimental prototype shows the beginning of a LEV, while none appears in the CFD. At the next instant, the LEV A is well visible in both approaches while the LEV B is transported well past the turbine. At instant (iv), the LEV A is well detached and induces some positive vorticity at the surface of the upper side. The positive vorticity sheet shed at the trailing edge of the lower surface also appears. Finally, at time (v), the LEV is over the trailing edge, helping the foil to pitch in the opposite direction.

For the high confinement case $c/H = 0.24$, the sequence shows several differences between the experimental and the numerical vorticity fields. However, one must recall from Figures 5 and 6 that the frequency of oscillation is not the same between both approaches, nor is the pitch amplitude and the

phase angle. Therefore, direct comparison between the visualizations at given fraction of the oscillation period is not possible. The smaller pitch amplitude on the prototype delays the moment at which the LEV is generated. For instance, at time (iv), the LEV is fully developed in the simulation and starts interfering with the heaving motion, preventing the foil from reaching the same amplitude as the prototype at the same instant. At time (v), the LEV on the prototype is fully developed. Also, the leading edge of the foil at that moment is only about 0.7 chords from the lateral wall. Consequently, it is possible that the proximity between the wall and the LEV affects its dynamics. The synchronization between the foil and the LEV is known to be critical to help the foil reverse its pitch angle. The possible desynchronization suspected in the experiments could diminish the pitching amplitude and delay the instant where the LEV is created on the next cycle. In the simulation, the LEV has already been generated and transported away. The simulated foil has reached a smaller amplitude in heave, so the interaction between the LEV and the wall may be minimal. The foil may not heave high enough in the simulation to get close enough to the wall and get its shedding synchronization disturbed as in the laboratory.

Currently, a few hypotheses are explored to explain the discrepancies observed between the experimental and numerical results at the highest confinement level $c/H = 0.24$. Turbulence modeling is one of the explored avenues since the Spalart-Allmaras turbulence model is formally a fully-turbulent high-Reynolds number model. A more appropriate turbulence model for the present Re=19,000 could perhaps predict more reliably the boundary layer detachment causing the shedding of the LEV. Another hypothesis is the proximity between the LEV and the boundary layers on the sliding lateral walls. Those in the laboratory start about 20 chords upstream of the passive blade while in the simulations, they are accounted for as slip walls, thus without boundary layers. As noted by Karakas and Fenercioglu [12] for their constrained OFT in confined conditions, the performances of the turbine increases with the confinement level. However, when the foil during its cycle approaches the wall at a distance of $d_w/c = 0.1$, the performance would drop in their setup. In our experiments, the foil gets at a distance of $d_w/c = 0.47$. It is estimated that the boundary layers on the lateral walls have a thickness of $\delta/c = 0.57$. One thus expects an interaction between the LEV and the boundary layer which may result in the generation of a secondary vortex at the wall, which in turn may interact with the LEV. Since the simulations use lateral slip walls, no secondary vortex can be created.

Conclusion

Three-dimensional URANS simulations at Reynolds number 19 000 have been conducted to replicate experimental results of a fully-passive oscillating-foil turbine in different confinement levels. Regarding the performances predicted by CFD, they match very well the increase in efficiency and in power coefficient as well as the observed pitching amplitude. Moreover, for the least confined configuration, corresponding to no sliding lateral walls in the laboratory channel, all the performance metrics match closely. At low confinement, the

vorticity field $\omega_z c/U_\infty$ from the CFD captures the main structures observed experimentally on the prototype. However, at high confinement, there is a significant mismatch in the LEV creation timing. Moreover, CFD shows an opposite trend regarding the heave amplitudes and the frequency as the confinement level is increased. Overall, this numerical and experimental comparison is considered a success given the simplifications needed to make the CFD possible. Further works are planned to refine the numerical modeling and resolve the remaining discrepancies.

References

[1] T. Kinsey *et al.*, "Prototype testing of a hydrokinetic turbine based on oscillating hydrofoils," *Renew. Energy*, vol. 36, no. 6, pp. 1710–1718, Jun. 2011, doi: 10.1016/j.renene.2010.11.037.

[2] J.-C. Veilleux and G. Dumas, "Numerical optimization of a fully-passive flapping-airfoil turbine," *J. Fluids Struct.*, vol. 70, pp. 102–130, Apr. 2017, doi: 10.1016/j.jfluidstructs.2017.01.019.

[3] E. Gauthier, T. Kinsey, and G. Dumas, "Impact of Blockage on the Hydrodynamic Performance of Oscillating-Foils Hydrokinetic Turbines," *J. Fluids Eng.*, vol. 138, no. 9, p. 091103, Sep. 2016, doi: 10.1115/1.4033298.

[4] H. Ross and B. Polagye, "An experimental assessment of analytical blockage corrections for turbines," *Renew. Energy*, vol. 152, pp. 1328–1341, Jun. 2020, doi: 10.1016/j.renene.2020.01.135.

[5] T. Kinsey and G. Dumas, "Impact of channel blockage on the performance of axial and cross-flow hydrokinetic turbines," *Renew. Energy*, vol. 103, pp. 239–254, Apr. 2017, doi: 10.1016/j.renene.2016.11.021.

[6] S. Mann, G. Dumas, and P. Oshkai, "Effect of Confinement on the Hydrodynamic Performance of a Fully- Passive Oscillating-Foil Turbine," p. 10, 2022. To be presented at the 7th International Conference on Jets, Wakes and Separated Flows, ICJWSF-2022, March 15-17, 2022, Nihon Univ., Tokyo, Japan.

[7] D. Iverson, "Experimental Investigation of Oscillating-Foil Technologies," M.Sc. thesis, University of Victoria, Victoria, 2018.

[8] M. Boudreau, G. Dumas, M. Rahimpour, and P. Oshkai, "Experimental investigation of the energy extraction by a fully-passive flapping-foil hydrokinetic turbine prototype," *J. Fluids Struct.*, vol. 82, pp. 446–472, Oct. 2018, doi: 10.1016/j.jfluidstructs.2018.07.014.

[9] T. Kinsey and G. Dumas, "Three-Dimensional Effects on an Oscillating-Foil Hydrokinetic Turbine," *J. Fluids Eng.*, vol. 134, no. 7, p. 071105, Jul. 2012, doi: 10.1115/1.4006914.

[10] M. Boudreau, M. Picard-Deland, and G. Dumas, "A parametric study and optimization of the fully-passive flapping-foil turbine at high Reynolds number," *Renew. Energy*, vol. 146, pp. 1958–1975, Feb. 2020, doi: 10.1016/j.renene.2019.08.013.

[11] M. Olivier and O. Paré-Lambert, "Strong fluid–solid interactions with segregated CFD solvers," *Int. J. Numer. Methods Heat Fluid Flow*, vol. 29, no. 7, pp. 2237–2252, Jul. 2019, doi: 10.1108/HFF-09-2018-0497.

[12] F. Karakas and I. Fenercioglu, "Effect of Side-Walls on Flapping-Wing Power-Generation: an Experimental Study," *J. Appl. Fluid Mech.*, vol. 9, no. 6, pp. 2769–2779, Nov. 2016, doi: 10.29252/jafm.09.06.25997.